The Effect of He Implantation on the Tensile Properties and Microstructure of Cu/Fe Nano-Bicrystals

Peri Landau, Q. Guo, K. Hattar, and J. R. Greer*

In situ uniaxial tensile experiments on as-fabricated and helium-implanted 100 nm-diameter Cu/Fe bicrystals unearth the effect of individual face-centred-cubic/body-centred-cubic (fcc-bcc) interfaces on improving radiation-damage tolerance and helium absorption. Arrays of nanotensile specimens, each containing a single Cu grain in the bottom half and a single Fe grain on top, were fabricated by templated electron-beam lithography and electrodeposition. Helium is implanted at 200 keV to a dose of 10^{14} ion/cm^2 nominally into the interface region. High-resolution, site-specific transmission electron microscopy (TEM) and through-focus analysis reveal that the interfaces are nonplanar and contain ≈5 nm-spaced He bubbles with diameters of 1–2 nm. Nanomechanical experimental results show that the irradiated samples exhibit yield and ultimate tensile strengths more than 60% higher than the as-fabricated ones, while they retain comparable ductility. Tensile failure always occurs gradually, along the interfaces, with no noticeable shape localization. The absence of brittle failure in He-irradiated metals might be explained, in part, by the inability of the small He bubbles to serve as sufficient stress concentrators for cracking. In addition, the non-orthogonal orientation of the interfaces with respect to the loading axes results in the development of both normal- and shear-stress components. Tensile loading along the pillar axes may cause those interfacial regions subjected to normal stresses to detach, while the inclined regions, subjected to shear, to carry plastic deformation until final fracture.

1. Introduction

An emerging focus to utilize the next generation of nuclear energy technology as a viable source of power requires significant materials research and development due to the demanding service conditions. These harsh environments include high-dose neutron bombardment, exposure to high temperatures and corrosive environments, and shock induced degradation, all of which pose a significant challenge for structural materials.[1]

During irradiation, energetic particles displace atoms from their lattice sites, which triggers collision cascades and forms irradiation-induced defects such as self-interstitials and vacancies. These defects interact among themselves, forming vacancy clusters, dislocation loops, and voids, all of which can cause structural deterioration.[1–3] Helium (He) production is often an inevitable by-product of radiation.[2] The limited solubility of He in metals has been reported to lead to the formation of bubbles and voids, which can cause embrittlement, void swelling and blistering.[4–7] In order to create radiation-tolerant materials that can withstand the extreme operating conditions, a fundamental understanding of the effect of radiation-induced defects on the mechanical behavior of the irradiated microstructure is needed. Novel material systems are required to promote the annihilation and recombination of point defects, suppress bubble formation and prevent blistering and void formation.

Different types of boundaries, such as coherent interfaces like grain and twin boundaries,[8] and incoherent interfaces like nanolaminates and nanostructured alloys,[6,9–18] have been reported to serve as efficient sinks for radiation-induced defects. For instance, nanostructured ferritic Fe-Cr-based steels that contained ultrahigh densities of nanofeatures (Y-Ti-O) were shown to tolerate radiation-induced defects, both at room and higher temperatures. High densities (10^{23} m^{-3}) of He bubbles with diameters less than 2.2 nm were dispersed at the interfaces between the steel matrix and the fine scale Y-Ti-O precipitates, and never developed into voids, remaining stable during aging at 850–1000 °C.[6,7] It was concluded that the nanofeatures enhanced the recombination of self-interstitials and vacancies, hindered climb and glide of dislocations, and trapped the dissolved helium into nanometer sized bubbles. These bubbles were subsequently found to act as efficient defect sinks because they prevented the additional He atoms from condensing onto the grain boundaries, which would lead to material degradation. Multilayered composites, which contained a high density of alternating thin films with nanometer-sized thicknesses, such as Cu/Nb,[10,12,13,18] Ag/V,[15,16] and Cu/Mo,[14] have also demonstrated the ability to suppress bubble formation, especially in the finer-striated cases. Implanting 1 at% He into 5 nm and 2.5 nm-thick Cu/Nb nanolaminates resulted in the absence of any observable He clusters, while the same samples with 70 nm layer thicknesses

Dr. P. Landau, Dr. Q. Guo, Prof. J. R. Greer
Materials Science, California Institute of Technology
1200 E. California Blvd, Pasadena CA 91125, USA
E-mail: landaup@caltech.edu
Dr. K. Hattar
Radiation-Solid Interactions
Sandia National Laboratories Albuquerque
NM 87185, USA

DOI: 10.1002/adfm.201201776

and identical He concentration were found to contain numerous helium bubbles. Furthermore, 4 nm-thick multilayers did not exhibit blistering upon annealing, which implied an enhanced resistance to radiation damage.[10,12,17,18] Molecular-dynamics simulations provided the atomistic basis for such an improvement and showed that the excess atomic volume at Cu/Nb interfaces led to the He being trapped at the interfaces and rendered them preferred sites for vacancy-interstitial recombination.[3,19] Li et al.[14] reported that Cu/Mo interfaces reduced radiation-induced point defect density and improved radiation tolerance by trapping the He atoms at the interfaces, where its solubility was found to be several orders of magnitude larger than that in the monolithic metals. It was suggested that the bubbles were likely segregated to the interfaces because of the attractive elastic interactions between their stress fields. Wei et al.[15,16] demonstrated that decreasing the layer thickness from 70 nm to 5 nm in Ag/V multilayers implanted with 10^{17} He ions per cm^2 led to the suppression of the radiation-induced hardening. Nanoindentation experiments on as-fabricated Cu/Nb nanolaminates conveyed that their strengths and deformation mechanisms were controlled by the interlaminate spacing, with three distinct mechanisms driving the plastic deformation at each characteristic length scale.[20] Samples with the individual layers thicker than 75 nm exhibited a Hall–Petch like relationship, where the strength scaled up with the square root of the decreasing layer thickness up to ≈1.4 GPa. The same Cu/Nb samples with thinner layers were reported to deform via confined layer slip (CLS), where the increase in strength was explained by the high shear stresses required to propagate a dislocation glide loop confined to a single layer. Their strengths increased with decreasing layer thickness to give a peak strength of ≈2.6 GPa for the 2 nm thick layers. Single dislocation loops cutting through the interfaces were reported to govern the plastic response of the Cu/Nb multilayers with less than 2 nm individual film thicknesses, with the peak strength of ≈2.6 GPa.

Nanomechanical testing of micro- and nanosized cylindrical sample geometries has helped uncover some of the physical mechanisms of plasticity in metals.[21–25] Uniaxial deformation experiments and atomistic simulations on the micrometer- and sub-micrometer single-crystalline metals revealed the emergence of size-dependent strengths, which were also found to be a strong function of the initial microstructure, defect density, and loading path.[21,22,26,27] For example, single-crystalline metals exhibit a "smaller is stronger" trend through a power-law relation between strength, σ, and sample size, D, $\sigma \propto D^{-n}$.[21,23,24,28] A large number of studies on the face-centred-cubic (fcc) samples with diameters between ≈200 nm and several microns, and which contained initial dislocations, reported this exponent to be ≈–0.6.[21,22,24] This type of a size effect was attributed to the introduction of free surfaces, which activated unique deformation mechanisms, not characteristic of the same materials with macroscopic dimensions, such as dislocation avalanches leaving the pillar at the nearby free surface, also known as "dislocation starvation".[25] In contrast, uniaxial compression and tension experiments on cylindrical nanocrystalline Ni samples with 60 nm grains and diameters between ≈100 nm and 1.6 μm were characterized by a "smaller is weaker" strength-diameter dependence, possibly due to the grain boundary mediated deformation processes.[26] Microcompression experiments on the cylindrical micropillars created from the Cu/Nb nanolaminates, with the individual layers spaced at 40 nm and 70 nm, demonstrated that the size effect in these metallic systems was driven by the layer thickness (i.e., by the intrinsic as opposed to the extrinsic characteristic length scale). The peak strengths of the 500 nm-diameter pillars, which contained both 40 nm-spaced and 70 nm-spaced Cu/Nb layers oriented orthogonally to the loading direction were reported to be ≈1.5 GPa.[29] Microcompression experiments on 1.1 MeV proton-irradiated Cu nanopillars demonstrated that their compressive strengths were indistinguishable from their as-fabricated counterparts of equivalent sizes. 400 nm sample diameter was reported to define a transition from the "smaller is stronger" size effect regime to the lower bulk-level strengths.[30] Microcompression experiments have also been conducted on 500 nm-diameter pillars, which contained 70 nm, 5 nm and 2.5 nm-thick Cu/Nb nanolaminates, oriented orthogonally to the loading axes and implanted with 35 keV He ions, or 7 at% uniformly distributed throughout the length of the pillar. The samples whose interlayer spacings were on the order of the mean distance between the He bubbles demonstrated a factor of 2 reduction in the amount of strain-hardening caused by the irradiation, 0.5 GPa increase in 70 nm-thick layers compared with 0.2 GPa increase in 2.5 nm-thick layers.[12]

The described studies highlight the potential of the face-centred-cubic/body-centred-cubic (fcc-bcc) interfaces to serve as effective sinks and recombination sites for point defects and insoluble He. The micromechanical test specimens utilized in the aforementioned studies were carved with a focused ion beam (FIB) from the larger samples, which were irradiated prior to the small-scale specimen fabrication, and contained multiple interfaces. This allowed for ascertaining how the sink strength influenced the material's robustness against radiation damage. In addition to strength, the proximity of irradiation-induced defects to a sink may be a key factor in defining radiation tolerance. However, the microcompression experimental methodology on multilayered samples may not be well suited for probing the sink proximity effects systematically, because: 1) using the FIB to fabricate small-scale samples inevitably introduces additional defects into the surface;[31] 2) shaping the small-scale samples from the irradiated bulk sample may alter the defect distribution within the sample; and 3) the presence of multiple, closely spaced interfaces limit the spatial distributions of defects.

We report the tensile mechanical response of the as-fabricated and He-implanted cylindrical Cu/Fe bicrystals with the diameters of 100 nm and heights of ≈1 μm, each of which contained a single fcc-bcc interface. These Cu/Fe samples were fabricated by first patterning a sacrificial mask layer with an array of holes via e-beam lithography, followed by metal electrodeposition into the developed vertical pores.[32] Helium was implanted at 200 keV to a dose of 10^{14} ions per cm^2 to position its peak concentration close to the interface. Uniaxial tension experiments were conducted on the individual nano-bicrystals in a custom-built in situ nanomechanical instrument, SEMentor, to the point of failure. Microstructural analysis of the interfaces at the atomic level was conducted, and the effects of helium implantation on the yield and ultimate tensile strengths, as well as on the failure mechanism of the samples, are discussed.

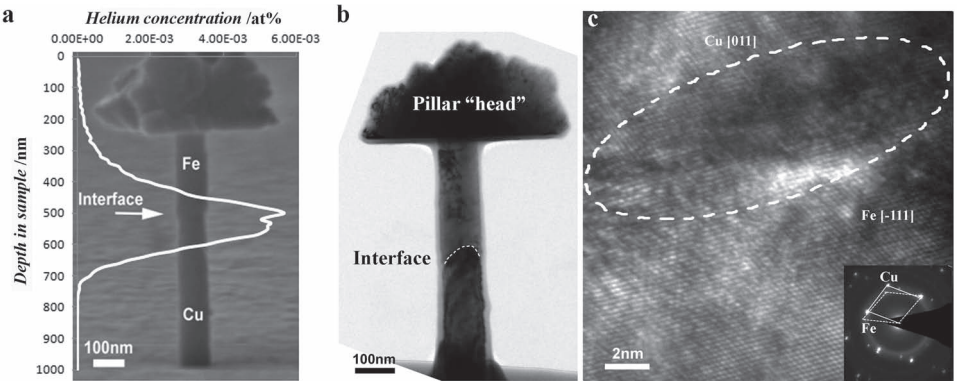

Figure 1. a) SEM image of a 100 nm-diameter Cu/Fe nanopillar combined with the He distribution according to SRIM calculations. The peak He distribution is around the interface (shown by the arrow in the image). b) Bright-field TEM image of a "plucked" pillar containing a wavy interface (marked by the dashed line) in a 100 nm-diameter Cu/Fe nanopillar. c) High-resolution TEM image of the interface with the corresponding diffraction pattern. The detailed atomic structure of the interface is obscured because of the wavy nature of the interface (the interface area is marked in the image).

2. Results

Figure 1a shows a scanning electron microscopy (SEM) image of a typical 100 nm-diameter Cu/Fe bicrystal with the arrow pointing to the interface. The bottom part of the pillar is comprised of single-crystalline copper, and the top part, which includes the overplated hat, is iron. Transmission electron microscopy (TEM) examination of the nanopillars revealed that the interface was sharply defined and slanted with respect to the loading axes, similar to observations by Guo and Greer.[33] These interfaces also appeared to be wavy, as shown by the dashed contour in the bright-field TEM image in Figure 1b. Most of the examined samples had close-to the so-called Kurdjumov–Sachs (KS) orientation, where the copper grew along its ≈<011> orientation, and the iron deposited close to its <111> direction. A high-resolution TEM image of the KS orientation part of the interface is shown in Figure 1c. A more-detailed analysis of the atomic structure of the interface was obscured by the interference caused by the nonplanar boundary topology.

The microstructure of the Cu/Fe samples after He implantation is shown in the TEM images in **Figure 2**. The novelty of these experiments required some extra characterization efforts. The evidence for the He bubble existence was obtained by through-focus imaging, a common technique for studying radiation damage,[34] which revealed the presence of 1–2 nm diameter He bubbles directly at the interface and in its vicinity, consistent with the lateral He distribution predicted by SRIM calculations.[35] In this case, the SRIM calculations likely overestimate the He penetration depth and represent its upper bound. This is because SRIM is typically used for implantations into continuous bulk materials and does not account for the possibility of He escaping from the pillar surfaces. Under-focus and over-focus images of bubbles in the vicinity of the interface are shown in Figure 2a,b, respectively. Figure 2c shows four under-focused bubbles at the interface, pointed to by the arrows. We found the appearance, size, and distribution of these He bubbles implanted directly into the nanopillars to be virtually identical to those in large-scale metals, as widely reported in the literature (see, for example Li et al. and Wei et al.[14,15]).

Time-lapse image series and load–displacement data, taken during an in situ tensile experiment of a typical irradiated pillar, are shown in **Figure 3**. Each image corresponds to a self-consistent marker in the load–displacement curve shown in Figure 3d. Engineering stresses and strains were calculated from the load–displacement data by using the initial cross-sectional area of the pillar and the initial gauge length (excluding the bottom glued part of the pillar), by assuming homogeneous deformation. This sample reached the yield stress of ≈760 MPa at the axial strain of ≈1.2%, and underwent ≈1% of plastic flow before reaching the ultimate tensile strength (UTS) of 960 MPa (Figure 3b). Failure of the pillar occurred after a gradual decrease in the force between the displacements of 12 and 46 nm. We expected such a stress–strain signature to be attributed to the formation of a neck, as has been reported during tension of

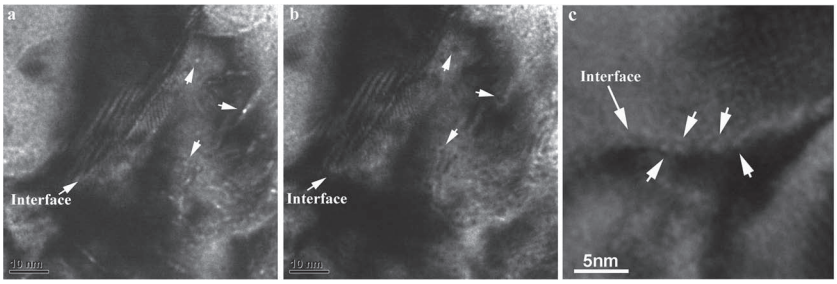

Figure 2. TEM images of He bubbles in the close proximity of the interface and at the interface were taken using the through-focus technique: a) under-focus image of He bubbles. The He bubbles appear as bright dots with a dark Fresnel fringe around them. b) Over-focus image of the same area. The bubbles appear as dark dots with a white Fresnel fringe around them. The same He bubbles are shown by arrows in the images. c) Under-focus image of He bubbles at the interface (shown by the arrows on the micrograph). The location of the interface is indicated in each micrograph.

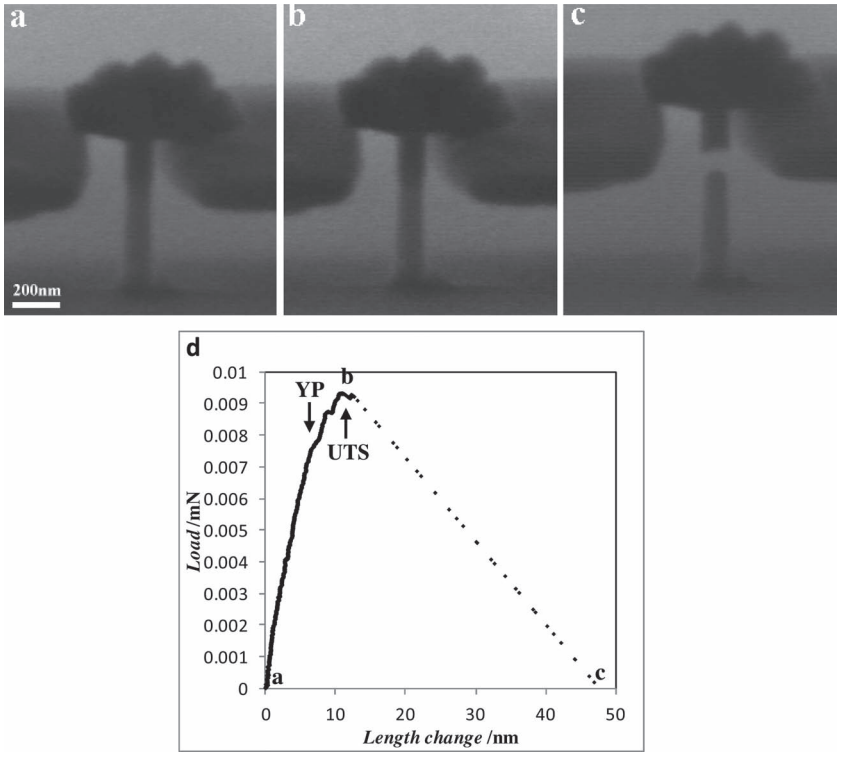

Figure 3. Snapshots from an in situ tension experiment: a) 100 nm-diameter Cu/Fe pillar at the beginning of tension experiment. b) The same nanopillar after reaching maximum load. c) Fractured pillar. Each snapshot corresponds to a different point in the load–displacement curve shown in (d) and marked on the curve. Post-UTS deformation is characterized by a rapid decrease in load with increasing length change until fracture.

pure Cu nanopillars produced and tested by the same methodology.[36] Based on our currently available observations, no apparent necking was observed in these interface-containing samples. Close analysis of the failed samples via high-resolution SEM imaging indicated that no visible diameter reduction in the interfacial area had occurred (Figure 3c). Other methods are currently being pursued to characterize the severed interfacial region in more detail.

Figure 4 contains the plots of the engineering stress–strain data for 4 of the tested as-fabricated and He-implanted 100 nm-diameter Cu/Fe bi-pillars (2 representative curves for each state). Conducting these experiments was non-trivial, which resulted in the total number of tested samples, 8, to be relatively low. Separate curves for the as-fabricated and the implanted pillars for all of the experiments performed can be found in the supporting information, along with the complete data set for all 8 curves (Supporting Information, Figure S1). The stress–strain signature for both types of samples is similar, characterized by some post-yield plastic flow before reaching UTS. The scatter in the initial loading slope is likely a result of the non-ideal alignment between the tensile grips and the pillar "mushroom" head, as well as the surface roughness. It is common for the initial portion of the data to be affected by a slight mutual misalignment between the bottoms of the pillar hats and the instrument grips in small-scale uniaxial tensile experiments. The equivalence of the stress–strain response past the strain of ≈0.5% in all of the samples studied, both implanted and as-fabricated, suggests that once full contact was established, the deformation was self-consistent, and the sample-to-sample variation in the data was marginal. It is possible that some of the change in the loading slope could arise from other factors, like changes in the material properties or in the interface topology, however the amount and the nature of the data spread are insufficient to conclusively confirm or renounce this claim. All of the samples experienced at least one displacement burst before reaching UTS, similar to the reported tensile engineering stress–strain curves of pure Cu.[36] The UTSs of the implanted bicrystals, ≈900 MPa, were found to be nearly a factor of 2 higher than those of the as-fabricated ones, ≈550 MPa. The plastic flow region in the implanted samples occurred between the displacements of 6 and 10 nm. This amount of plastic flow was measured to be ≈40% lower than that in the as-fabricated samples, while the overall elongation decreased by only 10%, as determined by the data produced by the nanoindenter combined with image analysis of in situ experiments. Both types of pillars failed gradually at the interface without any noticeable necking or strain localization.

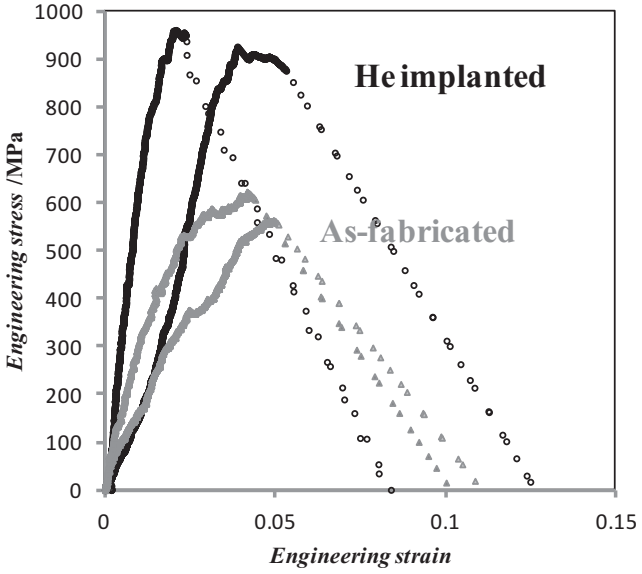

Figure 4. Representative engineering stress–strain curves of He implanted and as-fabricated 100 nm-diameter Cu/Fe nanopillars that contain a single interface. The variation in elastic modulus in both as-fabricated and implanted pillars can be attributed to either non-ideal alignment between the tensile grip and the pillar "mushroom" head and between the pillar and the substrate or to various surface imperfections formed during pillar growth.

3. Discussion

In situ uniaxial tensile experiments revealed that the engineering stress–strain data for the as-fabricated and He-implanted 100 nm-diameter Cu/Fe samples were similar to each other in that they contained an elastic loading segment followed by an average of ≈2% of plastic flow up to the ultimate tensile strength (UTS), with a subsequent gradual load removal to the point of failure. These stress–strain curves resembled the tensile behavior of pure copper samples with similar diameters, which were fabricated and tested by a similar methodology and tested in the same instrument.[36] The ultimate tensile strengths of such pure Cu samples were reported to be higher than those of both types of pillars studied in this work: by a factor of 3 compared with the as-fabricated interface-containing pillars and by a factor of 1.5 than the implanted pillars.[36] Such a reduction in strength in the interface-containing pillars, both as-fabricated and implanted, compared to pure Cu is consistent with previously reported compression results.[33] Our results indicate that the He implantation into the interface-containing pillars led to a greater than 60% increase in the yield and the ultimate tensile strengths, both of which were still lower than those of pure Cu samples with equivalent diameters. A possible phenomenological explanation for the ductile failure and the lack of necking is that the He bubbles did not serve as stress concentrators for crack initiation and propagation. During tensile straining, the initial part of the plastic deformation in all of the interface-containing pillars was accommodated by the Cu part only and then encompassed the boundary. Such a sequential deformation has been reported for the compressive response of Cu-Fe nano-bicrystals.[33] Their ultimate tensile strengths corresponded to the onset of interfacial delamination at the stresses below the yield strength of 100 nm-diameter Cu crystals. Subsequent gradual load decrease to the point of fracture occurred without any noticeable localization in the sample shape, which suggests that it was gradually deforming and delaminating to the point of failure. During this gradual delamination, it is possible that the inclined parts of the interface that remained intact carried the plastic strain, while the normally loaded regions separated. Another possible mechanism of gradual detachment might be related to the local microplasticity in Cu around the interface prior to failure. Microplasticity is a bulk-level phenomenon in metals, where the local regions within the overall elastically deforming material experience plastic deformation.[37] Generally, this phenomenon requires the presence of a relatively dense dislocation substructure, which enables the motion of individual dislocations within this substructure prior to the macroscopic yield point.[37] Metallic samples with nanometer dimensions cannot accommodate such dislocation substructures because they would be extremely unstable and because the typical cell dimensions in the dislocation networks are larger than the external pillar dimensions. These arguments imply that microplasticity is an unlikely explanation for the lack of brittle failure in the irradiated nano-bicrystals.

In addition to the gradual failure mode, the interface-containing nanopillars became stronger when irradiated with He. The strengthening observed as a result of He implantation may be explained, in part, by Orowan's model of dispersed barrier hardening, where the interactions between the gliding dislocation loops and He bubbles drive the required applied stress.[13] We observed a uniform bubble distribution in the vicinity of the interface, consistent with the SRIM calculation of He distribution across the interface (Figure 1a). The He concentration calculated according to SRIM may be overestimating the bubble density since it does not take into account escape of He from the pillar surface. According to the dispersed barrier hardening model, the increase in yield strength can be determined by:[38,39]

$$\Delta\sigma = M\alpha\mu b\sqrt{Nd} \tag{1}$$

where N is the He bubble concentration, d is the bubble diameter, b is the magnitude of the Burgers vector, μ is the shear modulus, α is the defect cluster barrier strength, and M is the Taylor factor of 3.06 for fcc and bcc metals. However, the multiple uncertainties associated with the bubble density measurements using two-dimensional TEM images render the measurement of bubble concentration from TEM images impractical.[16] These ambiguities may include factors like whether all the bubbles have been observed, if the bubble shape is well defined, and how to account for the overlapping bubbles. We derived the He bubble concentration from Equation 1 according to the measured increase in yield strength and calculated the bubble spacing to be:

$$l_s = 1\Big/\sqrt{2Nr} \tag{2}$$

where r is the bubble radius.[16] The Orowan model predicts 18 nm to be the average He bubble spacing in the Cu constituent, calculated using the experimentally determined increase in the yield stress of 0.5 GPa, and the shear modulus of Cu of 46 GPa, b = 0.255 nm, d = 1.5 nm, and α = 0.25. These parameters have been commonly used to describe hardening in the weak obstacle-containing metals.[38] 18 nm is several times larger than the observed He bubble spacing of a few nanometers, as can be seen in Figure 2a,b. Such a discrepancy between the measured He bubble spacing and that estimated by Orowan's model suggests that additional factors may be contributing to the hardening of the Cu/Fe nano-bicrystals.

Generally, He bubbles are considered to be weak obstacles to dislocation motion as compared to the interstitial loops. However, they may not be weak obstacles in the absolute sense, especially since an increase in UTS is observed due to He implantation. Therefore, a better approach to estimate the bubble spacing in the Cu/Fe nanopillars may be the Friedel–Kroupa–Hirsch (FKH) hardening model, which accounts for the less extensive bowing of dislocations prior to the obstacle breakaway:[38,39]

$$\Delta\sigma = 1/8\,M\mu b d\,N^{2/3} \tag{3}$$

where all the parameters retain their meaning as in Equation 1. The such-calculated He bubble spacing of 5 nm was in agreement with that observed in the TEM images (Figures 2a,b). This suggests that the He bubbles may serve as relatively weak obstacles to dislocation motion, which gives rise to the observed higher strengths. Such a mean distance of 5 nm corresponds to ≈1% of the layer "thickness," defined as the height of each

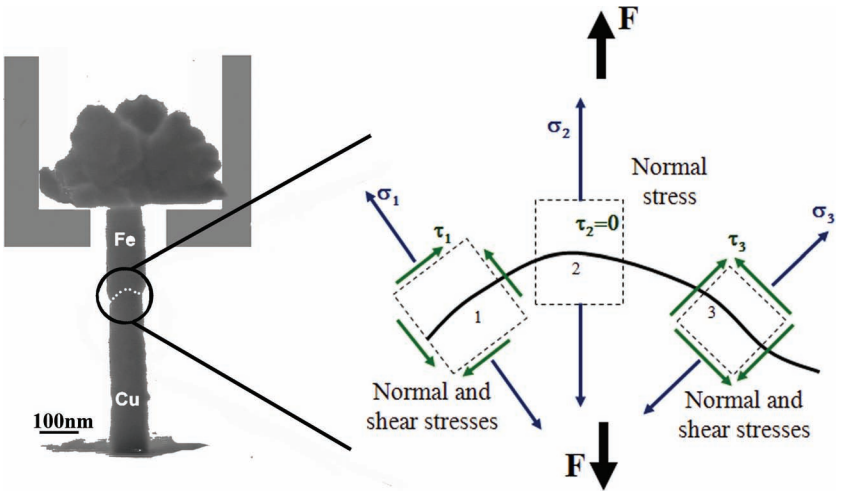

Figure 5. Schematic representation of the normal and shear stresses acting upon a wavy interface. The magnitude of the local shear and normal stresses is determined by the angle between the interface and the applied force such that $\tau_3 > \tau_1 > \tau_2$, as is schematically presented in the image.

subcrystal, close to 500 nm. This is in contrast with the ≈10% of the layer thickness in the 70 nm-thick Cu/Nb samples, which manifested twice as high relative hardening (60% increase in yield stress) between the as-fabricated and the irradiated samples.[12,16] This implies that the reduced hardening observed in multilayers, even at a thickness of 70 nm, is driven by the presence of multiple interfaces acting as sinks for He. The higher density of interfaces reduces the concentration of He bubbles in the matrix, which lowers the total number of obstacles within the matrix and leads to a less pronounced hardening. This suggests that the proximity of the He sink also plays an important role in eliminating radiation effects.

A marginal reduction in both the plastic flow and the overall elongation were observed during tension of the He-implanted samples compared to the as-fabricated ones. Typical bulk-sized metals irradiated with similar doses of He display significantly higher rate of hardening with a concurrent reduction in plastic flow followed by brittle failure at ambient temperatures.[40,41] In contrast, the single-interface containing nanopillars with ≈5 nm-spaced He bubbles concentrated near the interface studied here, became stronger and remained ductile as compared with their as-fabricated counterparts. We attribute such an improvement in the mechanical properties, in part, to the wavy interfacial topology. Similar nonplanar interfaces have been observed in sputter deposited V/Ag multilayers and explained by the kinetic constraints of deposition.[42] It was shown that the disconnections and the invariant habit planes were formed to relieve the mismatch strain along the interface. TEM analysis of the as-fabricated Cu-Fe nanopillar samples revealed that the fcc/bcc boundaries in most samples were oriented along the KS orientation, with the copper oriented along its ≈<011> orientation, and the iron oriented close to its <111> direction. The nonplanar interfacial regions experienced localized deviations from the KS orientation, forming discontinuities and invariants of habit planes. Such an incoherence of the interface may lead to the higher excess atomic volume within the boundary, making it an efficient sink for He atoms.

The wavy morphology of the interface may also explain the lack of necking instability during tensile failure. Both the He-implanted and the as-fabricated Cu/Fe nanopillars failed at the interface during tensile loading, and both sets of the stress–strain data indicated a reduction in the strained area until fracture, yet no tensile instabilities were observed. This can be explained by considering the full stress tensor generated along the interface in response to uniaxial normal loading. **Figure 5** schematically illustrates that in such an interface, whose internal regions are oriented at different angles to the loading axis, some parts of the interface experience a significantly higher relative normal stress component (i.e., oriented at 90° to the tensile axis), while others have a higher relative shear component. The local curvature of the interface determines the magnitude of the normal and the shear stress components at each locale. A higher angle between the normal to a particular planar section within the interface and the direction of the applied force results in a higher shear component, which would facilitate plasticity rather than fracture in these regions. These local shear processes, which commenced in the regions oriented non-orthogonally to the loading direction, likely suppressed the brittle failure. The remaining intact regions carried the plastic strain until the overall sample failure. Such a gradual reduction in the gauge area and the absence of embrittlement in the He implanted nano-bicrystals suggests that tuning interfacial topology may provide useful insights towards development of radiation-tolerant materials and that susceptibility to radiation damage may be a strong function of sink proximity in addition to sink strength.

4. Conclusions

Helium ions were implanted at 200 keV into 100 nm-diameter Cu/Fe nanotensile samples, each containing a single bicrystalline interface. The implantation led to the formation of 1–2 nanometer diameter, ≈5 nm-spaced helium bubbles concentrated at the boundary and within ≈50 nm of the interface. In situ uniaxial tension experiments revealed that the irradiated pillars had higher yield strengths by a factor of ≈2.5 and a higher UTS by 60% than the unirradiated ones, while retaining comparable ductility and without the appearance of brittle fracture. The hardening of implanted pillars is attributed to dispersion-strengthening in the Cu constituent of the sample. This is supported by the reasonable agreement between the mean He bubble spacing calculated by the Friedel–Kroupa–Hirsch hardening relation for weak obstacles and TEM analysis. The irradiation did not appear to alter the failure mechanism. These observations may be explained, in part, by the non-orthogonally oriented morphology of the interface, with the local interfacial regions oriented for shear deformation under prescribed loading carrying plastic strain prior to failure. The absence of brittle failure in He-irradiated metals is likely due

to the inability of the small He bubbles to serve as sufficient stress concentrators for cracking. These results shed light on the mechanical response and fracture behavior of a single interface and its role in absorbing He. Further examination of a controlled number of interfaces can determine the contribution of each interface to the improvement in radiation tolerance and resolve the effect of sink proximity on absorbing He.

5. Experimental Section

Bicrystalline Cu/Fe nanopillars were fabricated by electrodeposition of each metal into arrays of vertically aligned, 100 nm-diameter cylindrical holes patterned in the spin-coated poly(methyl methacrylate) (PMMA) film on a Si substrate coated with a thin gold film. The bimaterial pillars were created by using a dual-bath approach, where the Cu was first electroplated into the holes in PMMA on the Au film, and the bath was switched to Fe when the pillar height was approximately half of its final height. The details of this fabrication procedure are provided by Burek and Greer[32] and Guo and Greer.[33] These samples were intentionally over-electroplated to fabricate the mushroom-like hats on the tops of the pillars for tensile gripping. Figure 1a shows an SEM image of a typical tensile sample. The image illustrates that the total pillar height was ≈1 μm, and the distance between the interface and the pillar top was ≈500 nm. He ions with a beam energy of 200 keV and a dose of 10^{14} ions per cm^2 were implanted into the samples using an HVEE ion implanter at Sandia National Laboratories. Such irradiation conditions were predicted to cause a non-uniform distribution of He across the pillar height by SRIM simulation,[35] where a peak He concentration of ≈0.005 at% would be located at ≈500 nm from the top of the pillar, with a lateral distribution of 100 nm. The calculated distribution of He within the pillar gauge is overlaid on the SEM image of a typical sample in Figure 1a.

In situ uniaxial nanotension experiments of the implanted and as-fabricated Cu/Fe nanopillars were performed in the SEMentor, a custom-built nanomechanical instrument, comprised of a scanning electron microscope (FEI Quanta 200™ FEG) and a nanoindenter (DCM module, Agilent Corp.). All of the experiments were performed at a nominally constant displacement rate through a custom-written feedback-loop-based software method. The experiments were conducted in continuous stiffness mode (CSM), collecting instantaneous contact stiffness data throughout the experiment, which unambiguously detects the points of full contact between the tensile grips and the pillar top, as well as of failure. An example of the stiffness data collected during an experiment along with a time lapse series is provided in the supporting information. The actual elongation and strain were determined by correcting the raw length-change data, collected by the nanoindenter, which includes the effects of the instrumental compliance, etc., by the measured extension from the concurrently captured video frames (Supporting Information, Figure S2). To ensure repeatability, a total of 4 experiments for each state (as-fabricated and implanted) were performed in order to ensure repeatability, when experiments that showed misalignment between the tensile grip and the pillar "mushroom" head or bending during the experiment were not taken into account. All of the tensile experiments were performed with custom-milled diamond grips at a strain rate of 2×10^{-3} s^{-1}. Nanopillars for tensile experiments were attached to the substrate by localized e-beam deposition of a tungsten-containing organometallic compound using an FEI Nova 200 instrument, as described in detail by Jennings and Greer.[36] Some of the individual nano-bicrystals before and after deformation were lifted away from the parent substrate by using SEMentor grips and glued onto the TEM grids by W deposition for microstructural analysis. This sample-preparation technique did not require any additional thinning because the 100 nm-diameter samples were transparent to the electrons. Hence, no additional microstructural damage was accumulated – as would be the case with FIB-based preparation techniques. Site-specific microstructural characterization in a FEI Tecnai TF20 TEM was performed on the individual as-fabricated and implanted samples. The He bubble size and distribution were examined by through-focus imaging in the TEM.[34]

Supporting Information

Supporting Information is available from the Wiley Online Library or from the author.

Acknowledgements

The authors gratefully acknowledge the financial support of the US Department of Energy, Office of Basic Energy Sciences through JRG's Early Career grant. The authors also acknowledge support and infrastructure provided by the Kavli Nanoscience Institute (KNI) at Caltech and useful discussions with M. Demkowicz. P.L. thanks A. T. Jennings for help in mechanical data analysis. Helium implantation was supported by the Division of Materials Science and Engineering, Office of Basic Energy Sciences, US Department of Energy. Sandia National Laboratories is a multiprogram laboratory managed and operated by Sandia Corporation, a wholly owned subsidiary of Lockheed Martin Company, for the US Department of Energy's National Nuclear Security Administration under contract DE-AC04-94AL85000.

Received: June 28, 2012
Revised: September 11, 2012
Published online: October 12, 2012

[1] A. Misra, L. Thilly, *MRS Bull.* **2010**, *35*, 12.
[2] H. Trinkaus, B. N. Singh, *J. Nucl. Mater.* **2003**, *323*, 292.
[3] M. J. Demkowicz, A. Misra, A. Caro, *Curr. Opin. Solid State Mater. Sci.* **2012**, *16*, 101.
[4] T. Yamamoto, G. R. Odette, P. Miao, D. J. Edwards, R. J. Kurtz, *J. Nucl. Mater.* **2009**, 386.
[5] K. Farrell, S. T. Mahmood, R. E. Stoller, L. K. Mansur, *J. Nucl. Mater.* **1994**, *210*, 3.
[6] G. R. Odette, M. J. Alinger, B. D. Wirth, *Annu. Rev. Mater. Res.* **2008**, *38*, 471.
[7] G. R. Odette, D. T. Hoelzer, *JOM* **2010**, *62*, 9.
[8] M. J. Demkowicz, O. Anderoglu, X. Zhang, A. Misra, *J. Mater. Res.* **2011**, *26*, 14.
[9] E. G. Fu, A. Misra, H. Wang, L. Shao, X. Zhang, *J. Nucl. Mater.* **2010**, *407*, 3.
[10] K. Hattar, M. J. Demkowicz, A. Misra, I. M. Robertson, R. G. Hoagland, *Scr. Mater.* **2008**, *58*, 7.
[11] T. Hochbauer, A. Misra, K. Hattar, R. G. Hoagland, *J. Appl. Phys.* **2005**, *98*, 12.
[12] N. Li, N. A. Mara, Y. Q. Wang, M. Nastasi, A. Misra, *Scr. Mater.* **2011**, *64*, 10.
[13] N. Li, M. Nastasi, A. Misra, *Int. J. Plast.* **2012**, *32–33*, 1.
[14] N. Li, J. J. Carter, A. Misra, L. Shao, H. Wang, X. Zhang, *Philos. Mag. Lett.* **2011**, *91*, 1.
[15] Q. M. Wei, Y. Q. Wang, M. Nastasi, A. Misra, *Philos. Mag.* **2011**, *91*, 4.
[16] Q. M. Wei, N. Li, N. Mara, M. Nastasi, A. Misra, *Acta Mater.* **2011**, *59*, 16.
[17] X. Zhang, E. G. Fu, A. Misra, M. J. Demkowicz, *JOM* **2010**, *62*, 12.
[18] X. Zhang, N. Li, O. Anderoglu, H. Wang, J. G. Swadener, T. Hochbauer, A. Misra, R. G. Hoagland, *Nucl. Instrum. Methods Phys. Res., Sect. B* **2007**, *261*, 1–2.
[19] M. J. Demkowicz, D. Bhattacharyya, I. Usov, Y. Q. Wang, M. Nastasi, A. Misra, *Appl. Phys. Lett.* **2010**, *97*, 16.

[20] A. Misra, J. P. Hirth, R. G. Hoagland, *Acta Mater.* **2005**, *53*, 18.
[21] J. R. Greer, J. T. M. De Hosson, *Prog. Mater. Sci.* **2011**, *56*, 654.
[22] J. R. Greer, D. Jang, J. Kim, M. J. Burek, M. J. Burek, *Adv. Funct. Mater.* **2009**, *19*, 18.
[23] J. R. Greer, J. Kim, M. J. Burek, *JOM* **2009**, *61*, 12.
[24] A. T. Jennings, J. R. Greer, *J. Mater. Res.* **2011**, *26*, 22.
[25] J. R. Greer, W. C. Oliver, W. D. Nix, *Acta Mater.* **2005**, *53*, 6.
[26] D. Jang, J. R. Greer, *Scr. Mater.* **2011**, *64*, 1.
[27] A. T. Jennings, M. J. Burek, J. R. Greer, *Phys. Rev. Lett.* **2010**, *104*, 13.
[28] J. R. Greer, *Rev. Adv. Mater. Sci.* **2006**, *13*, 59.
[29] N. A. Mara, D. Bhattacharyya, J. P. Hirth, P. Dickerson, A. Misra, *Appl. Phys. Lett.* **2010**, *97*, 2.
[30] D. Kiener, P. Hosemann, S. A. Maloy, A. M. Minor, *Nat. Mater.* **2011**, *10*, 8.
[31] D. Kiener, C. Motz, M. Rester, M. Jenko, G. Dehm, *Mater. Sci. Eng. A.* **2007**, *459*, 262.
[32] M. J. Burek, J. R. Greer, *Nano Lett.* **2010**, *10*, 1.
[33] Q. Guo, J. R. Greer, *Scr. Mater.* **2012**, *66*, 5.
[34] M. L. Jenkins, M. A. Kirk, in *Characterization of Radiation Damage by Transmission Electron Microscopy*, Intitute of Physics Publishing Ltd. **2001**.
[35] J. Ziegler, *The Stopping and Range of Ions in Matter (SRIM)*, **2011**, available from: http://www.SRIM.org (accessed October 2012).
[36] A. T. Jennings, J. R. Greer, *Philos. Mag.* **2011**, *91*, 7.
[37] *Microplasticity*, (Ed.: C. J. McMahon), Interscience, New York **1968**.
[38] S. J. Zinkle, Y. Matsukawa, *J. Nucl. Mater.* **2004**, *329–333, Part A*, 88.
[39] N. Li, M. S. Martin, O. Anderoglu, A. Misra, L. Shao, H. Wang, X. Zhang, *J. Nucl. Mater.* **2009**, *289*, 233.
[40] H. Ullmaier, J. Chen, *J. Nucl. Mater.* **2003**, *318*, 228.
[41] P. Jung, J. Henry, J. Chen, J.-C. Brachet, *J. Nucl. Mater.* **2003**, *318*, 241.
[42] Q. Wei, A. Misra, *Acta Mater.* **2010**, *58*, 14.